A compact photoreactor for automated H_2 photoproduction: revisiting the (Pd, Pt, Au)/TiO_2 (P25) Schottky junctions

Pablo Jimenéz-Calvo [1,¥*], Mario J. Muñoz-Batista [2], Mark Isaacs [3], Xiaoyan Li [1], Miguel Ángel Muñoz-Márquez [4], Gilberto Teobaldi [5,6], Mathieu Kociak [1], Erwan Paineau [1*]

*Corresponding Author: pablo.jimenez-calvo@mpikg.mpg.de; erwan-nicolas.paineau@universite-paris-saclay.fr

[1] Université Paris-Saclay, CNRS, Laboratoire de Physique des Solides, 91405, Orsay, France
[2] Department of Chemical Engineering, Faculty of Sciences, University of Granada, Granada, Spain
[3] HarwellXPS, Research Complex at Harwell, Rutherford Appleton Lab, Didcot OX11 0FA, United Kingdom
[4] School of Science and Technology - Chemistry Division, University of Camerino, Via Madonna delle Carceri, 62032 Camerino, Italy
[5] Scientific Computing Department, STFC UKRI, Rutherford Appleton Laboratory, Harwell Campus, OX11 0QX Didcot, United Kingdom
[6] School of Chemistry, University of Southampton, Highfield, SO17 1BJ Southampton, United Kingdom
[¥] Department of Colloid Chemistry, Max-Planck-Institute of Colloids and Interfaces, Am Mühlenberg 1, 14476 Potsdam, Germany (present address)

ABSTRACT

The configuration and geometry of chemical reactors underpins the accuracy of performance evaluation for photocatalytic materials and, accordingly, the development and validation of thermodynamic and kinetic model reactions. The lack of accurate photonic, mass, and heat transport profiles for photochemical reactors hinder standardization, scale-up, and ultimately comparison between different experiments. This work proposes two contributions at the interface between engineering of chemical process and materials science: (A) an automated compact stainless-steel photoreactor with 40 cm^3 and 65 cm^2 of volume and area, respectively, for hydrogen photoproduction as a model reaction and (B) the synthesis, characterization, and performance of

TiO_2 Schottky junctions, using Pd, Pt, or Au nanoparticles (*ca.* 0.5, 1, 2wt.% loadings each) to validate the operation of the reactor. A photonic profile methodology is implemented to the studied reactor to obtain the local light absorption profile, opening up for evaluation of the local quantum yield calculation for the selected materials. A combination of transmission electron microscopy, (X-ray/ultraviolet) photoelectron/electron energy loss/infrared spectroscopies, X-ray scattering, inductively coupled plasma atomic emission spectroscopy, and ultraviolet-visible spectrophotometry is employed to determine the distinctive surface and bulk properties to build structure-function correlations. The (Pd, Pt, Au)/TiO_2 Schottky junction exhibits H_2 production rates slightly higher than previous studies, with quantum yields almost 2-fold higher than reported studies. These results, demonstrates that the proposed novel geometry of the photoreactor improves the photonic, heat, and mass profiles. An in-depth analysis of the Au plasmon was investigated coupling electron energy loss spectroscopy, UV-vis, and transmission electron microscope, resulting in insightful information about the Au NP mode at the TiO_2 interface.

Keywords: Photoreactor, photonic profile, Schottky junctions, TiO_2 P25, co-catalysts

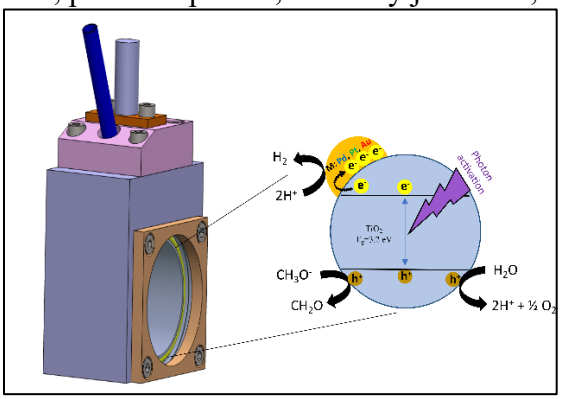

Solar energy[1–4] is foreseen as a promising solution of the climate crisis due its highly abundant energy content.[5] Capturing only 0.04% of the 36000 TW irradiation that arrives to the Earth' surface would be enough to supply the global energy demand, *e.g.,* 28 TW by 2050.[5] The photoconversion of solar photons to energy on demand has reached maturity in some technologies,

for example photovoltaics and/or concentrated solar power, but other tools are in current demand and development. One promising pathway to solar light conversion is by storing it in chemical carrier molecules[6] (molecular dihydrogen, H_2), easy to transport and straightforward to integrate in the existing technological transformation processes.[7] Amongst the solar fuels, H_2 is one of the most attractive systems due to its high mass-energy content (142 MJ/mol), two- to three-fold higher than conventional fossil fuels, when used in direct combustion.[5] H_2 is mainly produced by steam-methane reforming but renewables sources and processes are starting to appear in the roadmap.[8] By using the trifecta of light, water, and a catalyst (TiO_2) in 1972 Honda & Fujishima photoproduced H_2 via water splitting.[9] Since then, it has been five decades of active research in the field of artificial photosynthesis, referred by experts as one of the holy grails in physical-chemistry.[10]

Heterogeneous photocatalysis research into the H_2 evolution reaction (HER) requires the use of a suitable photochemical reactor along with the assistance of a sacrificial agent. It is noteworthy to say that the scaling-up of photocatalytic H_2 production has not reached a sufficient technological readiness level (TRL) due to a dual bottleneck: (A) efficient, abundant, recyclable, and low-cost catalysts and (B) a scalable, reproducible, and easy to handle reactor with a homogeneous photonic/heat/mass profile. Unfortunately, researchers have not yet developed photo catalytically active materials from cheap, abundant sources with the required ~10% solar-to-hydrogen energy conversion capacity[11,12] nor have we constructed a standard photochemical reactor of efficient photonic/heat/mass transfers with low losses. Therefore, the rational design of advanced photocatalytic systems has been the center of attention for several decades. However, the development of batch, scalable, and compact photoreactors has progressed more slowly compared with the advances made in photocatalytic materials discovery.[13] The design of compact and

transportable photoreactors comprising favorable properties (efficient local radiation/photonic flux, high photon absorption, homogeneous heat transfer, constant temperature during reaction, low volume, low mass of catalyst, good particle distribution) is of paramount importance for the TRL ascend towards achieving unprecedented thermodynamic and kinetic efficiencies. Of equal importance is the capability to perform operando and *in-situ* tests,[14–16] for better informed developments in the field. In this context, development of improved and better standardized photoreactors could reactivate interest and efforts in this perhaps the currently overlooked sub-field of photochemical engineering.

In terms of the photocatalytic materials design, multi-phase heterostructures in different organic/inorganic/metals (M) combinations have proven to surpass the efficiencies of their individual semiconductor (SC) components by modifying optical, electronic, morphological, structural, bulk, and surface properties.[17–19] Numerous multi-component composites have been reported and further progressed the semiconductor photocatalysis field. Regardless of these efforts, the benchmark material remains titanium dioxide (TiO_2), despite its wide band gap, *e.g.,* 3.2 eV[20] hindering the utilization of an important part of the solar spectrum, namely the visible one.[21] For that reason, titania-based materials have been rationally designed following different strategies – with the aim of improving visible-light capture properties. Examples include deposition of noble & coinage M (Schottky junction formation),[22–24] doping with impurities[25] (cation, anion, co-doped, and co-alloyed), coupling with medium or small band gap SCs (staggered/Z-scheme heterojunction formation),[11,17,18,26] and dye grafting[27,28] (surface activation and/or photosensitization).

Among the different TiO_2 band gap engineering modifications,[17,18,29,30] Schottky junction formation is particularly attractive because it exploits the use of deposited metal (M) nanoparticles

(NPs) onto a substrate SC with a physico-chemical contact to form an intimate interface. This composite structure exploits first, the co-catalytic active sites and, second, the electron pump functionalities, driven largely by electronic properties. A third functionality can be expected in cases where the M NP of choice has a surface plasmon, defined as the collective coherent oscillation of free electrons upon irradiation of a specific photon energy.[31] In photo electrocatalysis M/SC combinations have been widely used due to their vast performance augmentations delivered by the M NPs, bringing significant improvements (≥10 fold) compared to the SC alone.[32] Purely electrocatalytic metal activity has been elucidated to form a volcano plot relative to the standard free energy of adsorption assuming a Langmuir adsorption isotherm.[33,34]

The present work highlights two contributions in interconnected sub-fields: (A) a newly designed compact photoreactor (**Fig. 1a**) for automated HER in the presence of a sacrificial agent with frontal irradiation (engineering of chemical processes) and (B) synthesis, characterization, and performance of TiO_2 Schottky junctions, using Pd, Pt, or Au nanoparticles (*ca.* 0.5, 1, 2wt.% loadings each) to validate the operation of the reactor (materials science). Our hope is to further stimulate the design of novel compact reactors and accelerate the TRL-development for photo electrocatalysis. Automated data acquisition and H_2 quantification at controlled intervals is made possible due to the inclusion of an in-line gas chromatographer into the experimental configuration with defined parameters. Details on the setup are provided in **Experimental section**. The circular wall geometry, in contrast to other reactors[30,35,36], is conceived to avoid accumulation of particles in any corners, which guarantees continuous and homogeneous circulation of the NPs. A flat compartment at the bottom of the reactor (the width of a magnetic stirrer diameter – 0.5 cm) prevents obstructions to the vortex flow and enables sufficient convection to maintain a homogeneous suspension of NPs. Both geometrical choices are chosen to increase the photon-NP

impact probability when entering from the quartz window. A second source of NP transport is included in the form of a cross sectional vortex from the N_2 line, entering at the top right-hand side of the reactor. When determining the thickness (or depth) of the cylinder, a compromise is required between suspended NPs concentration and their passage into the quartz window entrance, the gateway of the incoming photons. Yet, a parametric study on stirring speed, NPs concentration, sacrificial agent concentration/nature, N_2 flux rate, and monochromatic lights should be envisaged.

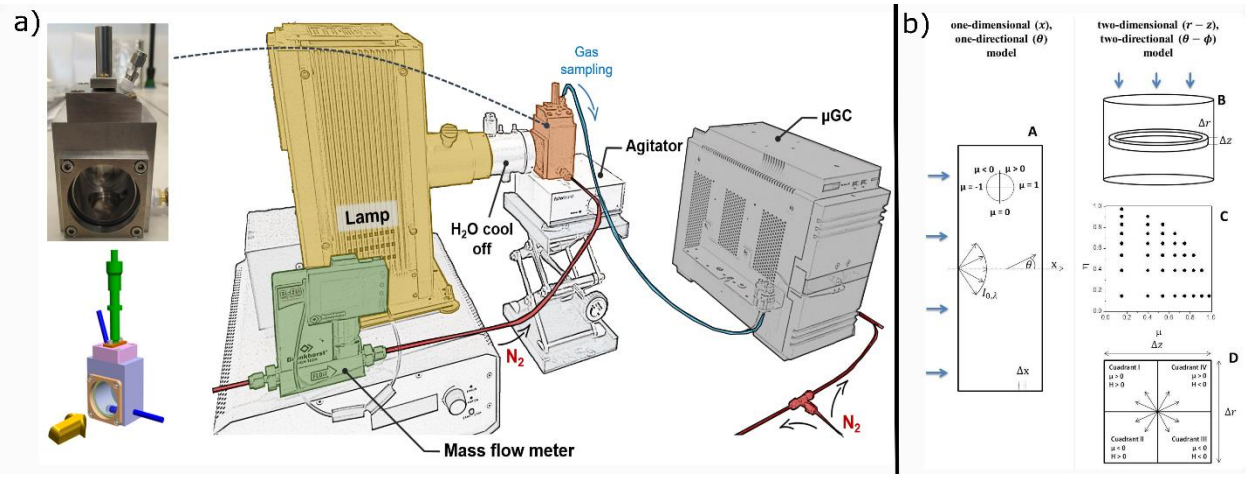

Figure 1. a) Compact photoreactor and its setup accessories **b)** Photonic local profile of the reactor showing the one-dimensional/one-directional radiation model (A) and two-dimensional, two-directional radiation (B-D). (B) Representation of the r and z spatial mesh discretization of the photoreactor, (C) Directional mesh for the Quadrant I and (D) representation of quadrants of the spatial cell.

Therefore, the implementation of a photonic model is of great use for two reasons: a) evaluate the photoreactor photonic transfer efficiency and b) to combine such functionality with the material's light absorption to obtain quantum yields. The light absorption capacity of the photoreactor is evaluated through a photonic model. Such model is well described elsewhere[14] even so it is implemented for our photoreactor contributing to its efficiency understanding. In short, the radiative transfer system (RTE, equation S1) is proposed assuming a set of defined physical properties and geometry conditions (see S1). The model combines the optical properties of the photocatalyst suspensions at different concentrations using the discrete ordinate method (DOM) in the rectangular spectrophotometer reactor. The reactor is considered as infinite plane parallel

medium with azimuthal symmetry, with one-dimensional and one-directional radiation transport model to solve the RTE (**Fig. 1b) A**). To apply the DOM tool to transform the integro-differential equation S1 into a system of algebraic equations, possible to solve numerically, our reactor configuration requires the use of a cylindrical two-dimensional (r-z variables), two-directional ($\theta - \phi$ variables) model of the photoreactor radiation field (**Fig. 1b) B-C**). The net radiation intensity at each $r - z$ point of the reactor is now represented using a discretized spatial mesh having two angular-related coordinates $\mu = \cos(\theta)$; $\eta = \cos(\phi)$. Fig. 1b) C displays μ; η unitary, basal projection(s) in a quadrant of the space around a $r - z$ point calculated using the S16 method.[37] The intensity obtainment at each point of the reactor require to divide the space in 4 quadrants as depicted in **Figure 1b) D** and the measurement of the incident light intensity at the boundary (liquid surface) using actinometry.[38] According to the Duderstadt and Martin recommendation and their propose numerical procedure[38], the finite difference and DOM was derived directly from the radiation balance for each mesh reactor (**Fig. 1b) D**). As a result of solving the algebraic system (elucidated in S1), the local volumetric rate of photon absorption ($e^{a,v}$) is calculated at each $r - z$ point of the reactor according to the integral:

$$e^{a,v} = \int_{\lambda} \kappa_{\lambda}(\underline{x}) \cdot \int_{\Omega=4\pi} I_{\lambda,\underline{\Omega}}(\underline{x}) d\Omega \, d\lambda$$

Details of the RTE and DOM approaches are given in supplementary information section.

The commissioning of this compact reactor is assessed by revisiting the well-studied Schottky junctions, in the benchmark TiO_2 (P25) containing noble M (Pd, Pt, or Au) NPs for validation. Such composites are synthesized via two-step chemical reduction methodology (**Fig. 2**, see

Experimental section). For each anchored M onto TiO_2, three loadings, *i.e.,* 0.5, 1, and 2 wt. % are implemented, standing for M0.5, M1, and M2, respectively, where M can be: Pd, Pt, or Au.

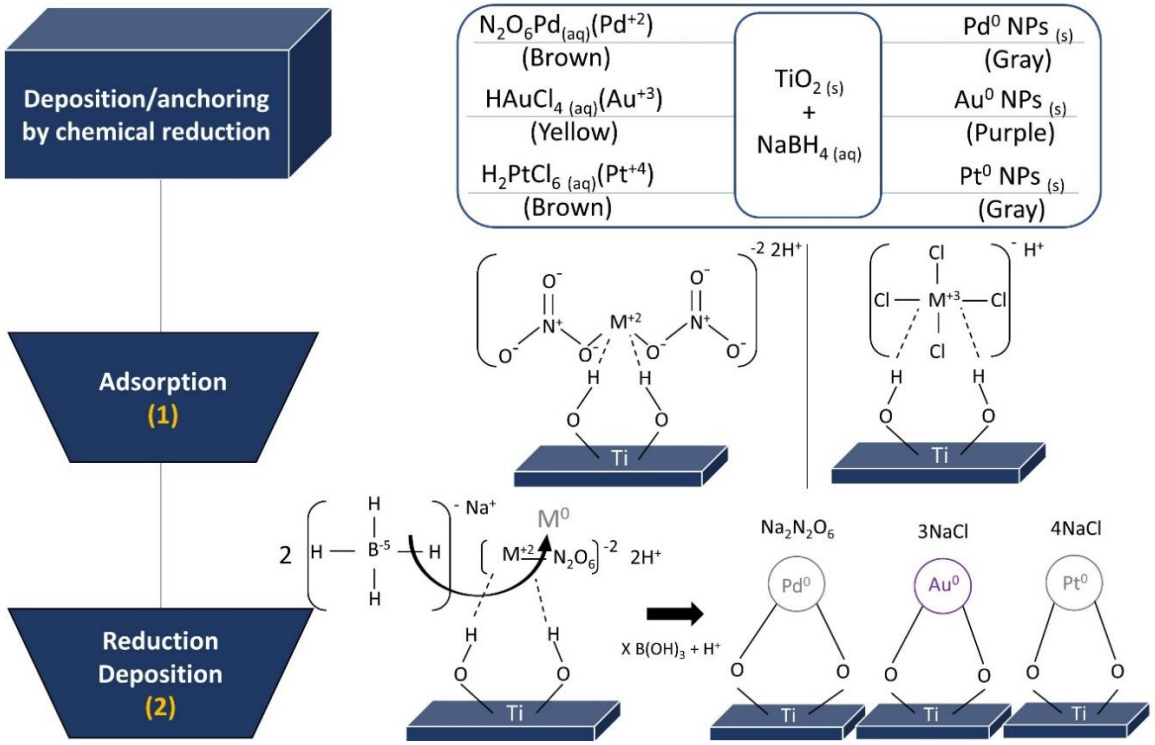

Figure 2. Illustrative scheme of the two-step chemical reduction deposition mechanism: adsorption of the M precursors followed by chemical reduction during the anchoring step.

Elemental analysis performed by inductively coupled plasma atomic emission spectroscopy (ICP-AES) indicates that the chemical reduction method ensures relatively high deposition yield (**Table S1**), while HRTEM analysis reports a good distribution of controlled size for each M NP systems (**Fig. 3**). The metal deposition yield onto TiO_2 ranges from 67 to 81% for all composites. It should be noted that the Au deposition yield (72-80 %), is higher than for Pd (70-74%) and Pt (67-71%), however this difference may be considered to be relatively minor, ensuring a reliable comparison for the photocatalytic H_2 production for each system.

The HRTEM micrographs in **Fig. 1** show the nine Schottky junction composites, three for each metal with equivalent loadings, namely Pd0.5, Pd1, Pd2 (**a-c**), Au0.5, Au1, Au2 (**d-f**), and Pt0.5,

Pt1, Pt2 (**g-i**). These images illustrate the typical grains of TiO_2 P25 with particulate diameters spanning a few tens of nm. Regarding the metal loadings, Pd, Pt, and Au NPs display a spherical morphology although a minor population of cylindrical NPs is also present for Pt. Pd (3.6-4.3 nm) and Pt (2.2-2.9 nm) particle size is found to exhibit a monomodal distribution, essentially independent of metal loading across the range of loadings prepared in this work (**Fig. S2**). Au/TiO_2 composites however, present a slight discrepancy in NP size (3.1-5.0 nm), with increasing loading. As we increase the loading from 0.5, through 1 and 2 wt.%, we observe an increase in particle size from 3.1 nm, through 4.3 nm, and up to 5.0 nm (**Table S1**). One can conclude that there is a quasi-linear trend of the Au NPs size by doubling and/or quadrupling its content, while the variance in particle size (**Table S1**) suggests reproducible growth of the Au NPs.

The Pd/TiO_2 binary samples display a relatively lower coverage along their surfaces than Au/TiO_2 homologues, and the distribution is preferentially located in specific regions; meaning that the Pd NPs preserve the number per area (in the regions they are present) despite doubling or quadrupling its content. The Pd/ (0.5, 1, and 2 wt.%)/TiO_2 materials yield an average size of 4.1, 3.6, and 4.3 nm (**Table S1**), evidencing that the method allows to maintain a narrow range of NPs sizes independently of the M content. Compellingly their associated standard deviation have 1.4-1.6 nm (**Table 1**) values, confirming a high degree of dispersity of the NPs sizes, *i.e.,* ranging from 1 to 7 nm, for the three loadings. A minor population of NPs (8 and 9 nm) are presented, possibly in charge of the high deviation value corroborating also the inhomogeneous coverage. The Pt/TiO_2 junctions displays a low and inhomogeneous coverage along the TiO_2 grains. Particularly, Pt presents a narrow NP size distribution with 2.2, 2.9, and 2.5 nm (**Table S1**) with the smallest standard deviation ranging from 0.6 to 1.1 nm. Such average NPs size are statistically equivalent, but their low deviation evidences the consistency on the NPs size in all the three composites, *e.g.,*

2.2-2.9 nm. Furthermore, one can conclude that the chemical reduction method for the junction system is consistent independently of the precursor used due to the monomodal particle size distributions for the three metals.

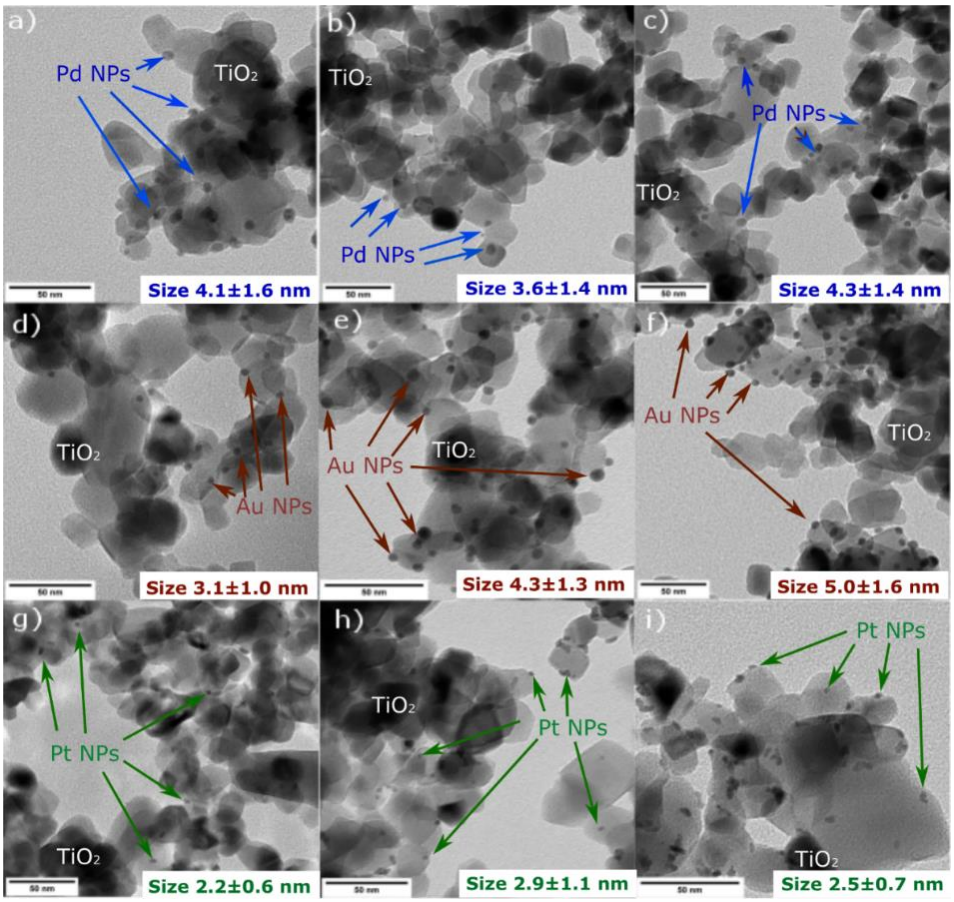

Figure 3. HRTEM images of the 0.5, 1, and 2 Pd/TiO_2P25 (a-c), Au/TiO_2P25 (d-f), and Pt/TiO_2P25 (g-i)

FT-IR spectroscopy is used to probe the influence of the three anchored Ms onto TiO_2 surfaces in different loadings. FT-IR spectra of all composites (Pd, Au, and Pt) and reference (bare TiO_2) (**Fig. S3**) exhibit the characteristic peaks of TiO_2. The major broad absorption band extending from 3000 to 3600 cm^{-1} observed in all 10 samples is attributed mainly to the asymmetrical and symmetrical stretching vibration of surface hydroxyl groups (O-H) but also to, a lesser extent, to physisorbed water species.[39] A doublet with similar intensity is present at ≈1620 cm^{-1} and ≈1400 cm^{-1} for all samples. The absorption band located at ≈1620 cm^{-1} is assigned to the bending vibration of Ti-OH

distorted by the adsorbed water molecules.[40,41] The absorption band located at ≈1400 cm^{-1} can be related to the accompanied by two weak bands at ≈2920 and 2850 cm^{-1}, due to the vibrational modes of organic species.[41] In general, the recorded spectra between the composites and the reference do not exhibit significant differences. Nonetheless, a slight shift to lower wavenumber after metal loading can be seen and tentatively related to hydroxyl bond weakening due to H-bond formation with the metals. Overall, these results suggest that the deposited M NPs do not influence drastically the TiO_2 lattice.

X-ray scattering (**Fig. S4**) of Schottky composites, a pristine TiO_2, plus calculated XRS diagrams of pure anatase and rutile phase uncover the structural properties of the composites. The diffractograms of TiO_2 P25 display well-resolved Bragg peaks corresponding to a mixture of anatase and rutile,[42] as expected. The scattering from TiO_2 particles is not affected by the choice of metal nor loading, suggesting that the formation of the M/Schottky junctions does not alter the crystal structure of bulk TiO_2. This is confirmed by estimating the coherent scattering length for the anatase crystallographic phase (101 plane), using the Debye-Scherrer equation. The average crystallite size (**Table S1**) for anatase (10.0-10.6±0.4 nm) does not vary by significant amount, while differences due the presence of metal crystallites may not be detected due to the low M concentration (according to HRTEM) since the metal NP diameters are not large enough to form Bragg peaks from $Mo_{k\alpha}$ X-rays.

UV-vis spectra of all samples (**Fig. S5**) display the typical absorbance maximum in the UV/blue range of TiO_2, ($\lambda_{absorption}$ = 386 nm)[43], equivalent to an approximate apparent band gap of 3.2±0.1 eV deduce by a Tauc plot. Au/TiO_2 composites alone produce a clear maximum centered at *ca.* 530 nm,[44,45] attributed to the well documented surface plasmon resonance (SPR) of Au NPs. The

SPR plasmon intensity correlates with metal loading, while an accompanying redshift in the peak maximum. Pt and Pd NPs do not exhibit an SPR in the visible range.

Surface analysis of the metal NPs was performed using X-ray photoelectron spectroscopy, to elucidate metal speciation and probe local chemistry. Survey spectra (**Fig. S6**) reveal the composites to be entirely Ti, O, C and the relevant metal. High-resolution scans of the Pd 3d, Au 4f and Pt 4f regions indicated an entirely metallic identity for all 9 materials. Pd 3d (**Fig. 4a**) and Au 4f (**Fig 4b**) scans may be characterised by the presence of single spin-orbit doublet (Pd $3d_{5/2}$ + Pd $3d_{3/2}$ and Au $4f_{7/2}$ + Au $4f_{5/2}$) of asymmetric character and were fit using modified Voigt-type lineshapes modelled from bulk metal standards. Platinum 4f (**Fig 4c**) also reports a single oxidation state of metallic, asymmetric peaks – though deconvolution is somewhat convoluted by the presence of an energy loss feature from Ti 3s photoemission. Quantification of the photoemission peaks revealed similar trends regarding surface:bulk ratios (**Fig. S7**) – that of a general inverse proportionality typical of nanoparticles on a surface.

UPS spectra (**Fig. S8**) allow determination of both valence band maximum (VBM) and work function (WF, **Fig. 4e**), whilst knowledge of the material band gap (deduced by Tauc plot) is made possible the calculation of the conduction band minimum (CBM), providing an energy band alignment diagram (**Fig. 4d**) including the oxidation-reduction potentials extracted from the Pourbaix diagram.[46] TiO_2 is not influenced optically nor structurally by anchoring of the M clusters. The resulting band gap indicates this clearly since all composites exhibit 3.2±0.1 eV value (**Fig. S5**). The first trend found is the significant VBM difference (0.23 eV) between pristine (-3.48 eV) and reduced TiO_2 (-3.25 eV), presumably due to the loss of surface hydroxyls after treatment with $NaBH_4$ in excess coupled with the sonication process. For all of the M/TiO_2 composites a concomitant increase in the VBM/CBM edge with loading is observed, following the

same argument of hydroxyls loss due to anchorage. The only exception to this trend is Au0.5 though this can be attributed to the less homogeneous Au nanoparticulate structural parameters, known to impart complex influence upon electronic properties.[47] In all cases, the inclusion of M NPs into the TiO_2 SC markedly enhances the VBM/CBM levels, confirming the M/SC interface.[48] Moreover, the resulting SC band edges can be evaluated against water redox potentials – all samples in principle can undergo the water oxidation, though photo reduction may be easier for the samples with higher M loading (2wt%) since these have higher VBMs relative to H^+/H_2 potential values compared to the low M loading samples. However, provided the M/SC interface junction is formed, some additional charge carrier pathways can exist and contribute to surpass the overpotentials (Schottky barrier) and promote the HER. This can be through an electron pump from the CB of the SC to the M NP or via hot electron injection from the SPR active Au NP to the TiO_2 CB.[49] The WF results (**Fig. 4e**) are firstly compared to the theoretical values of TiO_2 (4.6-4.7 eV), Au (5.10-5.47 eV), Pd (5.22-5.60 eV), and Pt (5.12-5.93 eV)[50,51] given the classic efficacy stated in the volcano plot Pt>Pd>>Au. The WF-value recorded for Pd and Pt are comparable to the theoretical values, while the one for Au is marginally higher than expected potentially the result of differences in strong metal-support interaction between the Au NPs and the TiO_2 support.[52] In the case of unmodified TiO_2, the WF values are 0.6-0.7 eV higher than those determined theoretically. However, the relative difference between the samples implies a stability of the overall electronic configuration during the reduction process. The Au WF values are above those for the Pt and Pd junctions. However, in general, the differences (0.1 eV) between the different M loadings are small, pointing to an overall electronic stability.

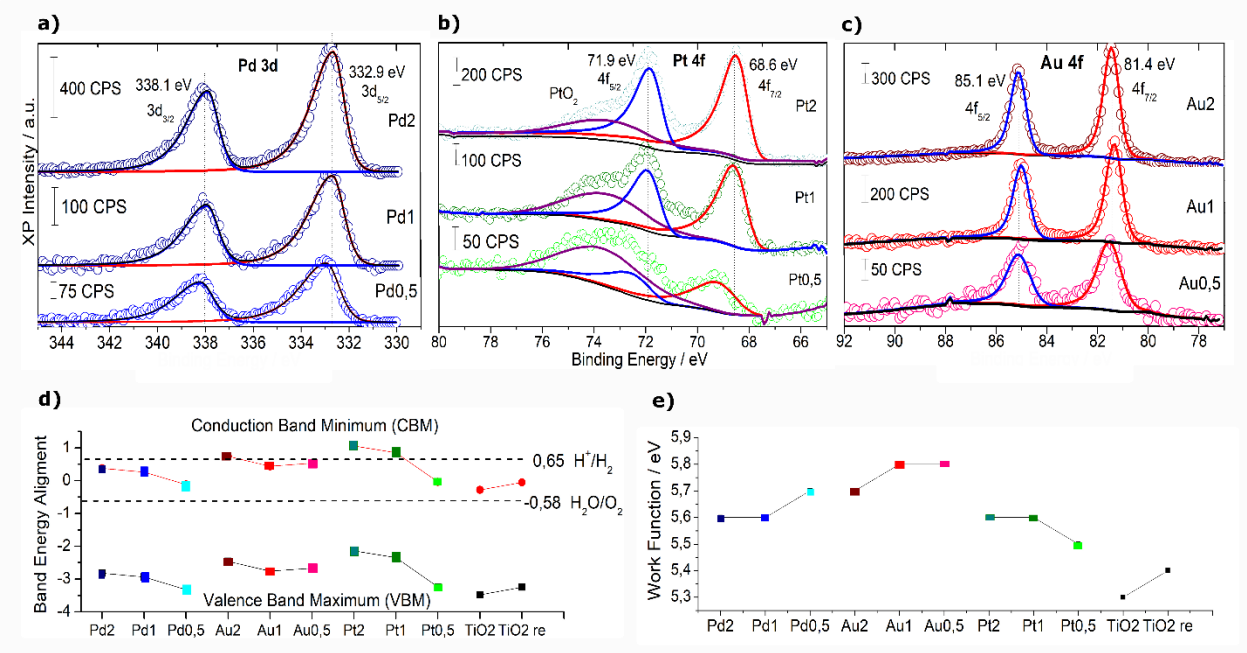

Figure 4. XPS spectra a) Pd 3d b) Pt 4f and c) Au 4f d) Band alignment diagram by coupling UPS and UV-vis e) Experimental work function of the 0.5, 1 and 2 wt.% (Pd, Pt, and Au)/TiO_2 composites.

The (Pd, Pt, and Au)/TiO_2 junctions result to be photoactive and their H_2 production follows the reactivity sequence of the noble metals: Pd>Pt>>Au, despite the metal loading.

Table 1. Summary of the data obtained from the cumulative HER, normalized H_2 formation rate, and quantum yield (Q.Y.) percent deducted from the photonic profile.

Sample	HER $\mu mol\ h^{-1}$	HER $mmol\ h^{-1}\ g_{cat}^{-1}$	Q.Y. %
Pd0.5	14174	7.5	7.3
Pd1	18993	10.2	9.9
Pd2	24505	12.6	12.3
Pt0.5	8467	4.2	4.1
Pt1	16316	8.1	7.9
Pt2	21075	10.4	10.1
Au0.5	3478	1.8	1.6
Au1	9732	4.9	3.4
Au2	13096	6.6	3.2

Fig. 5a-c and **table 1** shows the cumulative evolution of H_2 for all 9 composites. In all cases activity scales with M loading, with diminishing returns as loadings reaches 2%. These results demonstrate that the M identity plays a key role, though noteworthy is the determination that Pd NPs enhance the H_2 production process more than either Au or Pt – previously only observed for

single atom catalysts.[53] Hence, one can conclude that the intimate contact interface of the M and TiO_2, defined by the type of deposition, drives an efficient internal electronic communication via simple or numerous charge carrier pathways between the two moieties that ultimately leads to excellent, good or average photo activity.

By normalizing the H_2 results (**Fig. 5b, table 1**) with the mass of catalyst allows to see the same trend as for the cumulative H_2 for all samples, as expected. 2 wt.%Pd exhibits the highest HER rate, *ca.* 12.6 mmol g_{cat}^{-1} h^{-1}. In general, for all the Schottky junctions the normalized H_2 photoproduction rates are slightly higher compared with reported literature[53–59], confirming that at comparable experimental conditions, the use of this compact reactor enhances the HER efficacy of the studied benchmark materials.

By comparing the cumulative HER curves (**Fig. 5c, table 1**) of only the higher M loadings, the Pd-loaded systems emerge as the more efficient, resulting in a production of 608 mL of H_2 in 3h, which (assuming a good stability over time) extrapolated in time would produce 1L of H_2 after 2 continuous days. Contrastingly, for the Au junction, four days would be required to produce the same amount of H_2.

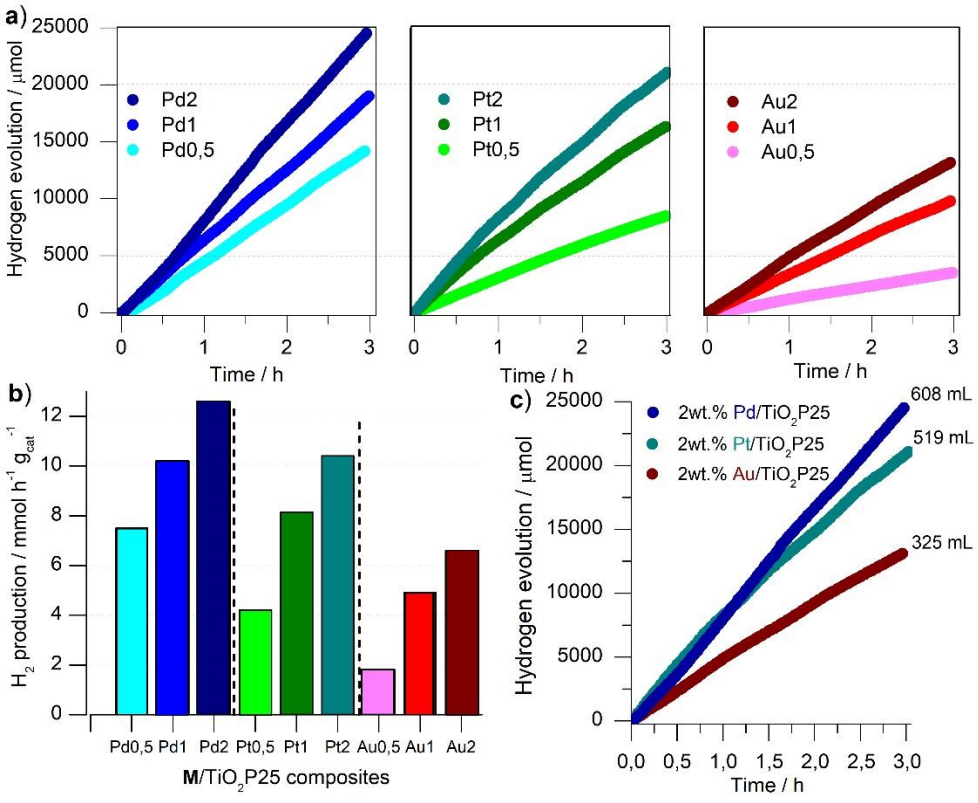

Figure 5. a) Cumulative evolution of hydrogen with 30 vol% of methanol under solar light for the 0.5, 1 and 2 wt.% (Pd, Pt, and Au)/TiO_2 Schottky junctions **b)** Mean hydrogen formation rate per hour per mass **c)** Cumulative evolution of hydrogen of 2 wt.% (Pd, Pt, and Au)/TiO_2 composites with their equivalent liquid hydrogen production.

Table 2 compares a few works on semi-equivalent Schottky systems but tested in different reactors to contextualize the H_2 photoproduction results of this study. The M-based composites are also anchored in TiO_2, not necessarily P25 but anatase, rutile, brookite, or a combination of the mentioned. The analysis is focus on two efficiency factors, *ca.* HER and Q.Y. but support (TiO_2), yet material modification and reactor conditions are pointed out to have a better overview of comparison. The (Pd, Pt, Au)/TiO_2 Schottky junction exhibits H_2 production rates slightly higher than previous studies, with quantum yields almost 2-fold higher than reported studies. These

results, demonstrates that the proposed novel geometry of the photoreactor improves the overall photonic, heat, and mass profiles, lowering the losses contribution.

Table 2. Comparison of photocatalytic efficiency for the TiO_2-based materials tested at similar reactor experimental conditions.

Efficiency		TiO_2 material				Reactor conditions				Ref.
HER mmol h^{-1} g_{cat}^{-1}	Q.Y.	M	%	Pre- or Post-treatment	Method	S. Agent	%	Lamp	Time h	
0.7	N.r.	Pd	1	-	-	MeOH	50	365 nm	5	[53]
2.2		Pt								
0.5		Au								
1.5	0.1	Au	0.3	Pre	Calcined	TEOA	1	150 W	2.5	[54]
3.0	1.7	Pd	1	Pre	Nb-doping, drying, calcined	MeOH	30	500 W	3	[56]
	2.0	Pt	1							
2.4	N.r.	Au	1	Post	Calcined	MeOH	50	7.2 W	3	[57]
1.8	1.0	Pt	0.5	Pre	Calcined	MeOH	30	500 W	3	[58]
0.06	N.r.	Au	1	-	-	MeOH	50	1000 W	4	[59]

N.r. = not reported, MEOH = methanol, TEOA = triethanolamine

The local photonic absorption profiles (**Fig. 6a**) for the 2% samples reveal that Pt and Pd have a similar light absorption to that of TiO_2 P25, as expected and confirmed by the comparable UV-vis spectra. The 2%Au/TiO_2 however, increases its light absorption, essentially in front of the quartz window, enhancing capture efficacy of incoming photons compared with its Pd and Pt analogues. It is noteworthy to mention, that although the photons are the source of activation for the SC, this does not necessarily mean that all the absorbed photons will end up in useful excitons and from there separate charge-carriers that can transform the reacting molecules. To associate the photonic model implementation and the chemical conversion (H_2 photoproduction rate) the quantum yield is determined (**Fig. 6b**). The series of junctions follow the quantum yield (QY) sequence of the noble metals: Pd>Pt>>Au, in a linear trend with cumulative reactivity. Interestingly, the obtained QYs are notably higher compared with reported results[53–59] (at least double), verifying that for

similar experimental conditions, the compact photoreactor enhances the mass/heat transport phenomena and exposure to light. Such enhancement favoured transport-limited processes, resulting in a controlled assessment of the activity performance. In general, QY is found to be intrinsically related to metal content – with the exception of Au 2% (potentially due to diminishing enhancements from larger particle sizes). These results demonstrates that light absorption (density of absorbed photons) is not the only parameter influencing the material's activity[54] and that charge generation/separation/transport plays a key role. In addition, one cannot discount that accessibility to the active sites also dictates the efficiency of surface reactions. Therefore, this result paves the way to further questions regarding the quality of the interface between the Au NP and their support. To this end, energy electron low spectroscopy (EELS, **Fig. 6c**) is carried out to better understand the mode/interaction present on a single Au NP and its support. The plasmon energy value is known to drastically depends on the electromagnetic environment of the NP that subtends it.[60] One single NP deposited on a substrate (TiO_2) is likely to exhibit dual energy modes: a plasmon mode localized at the substrate vicinity (evidencing the M/SC interface formation), another a plasmon mode localized at the vacuum interface. Eventually the mode localized at the vacuum NP interface (2.43±0.01 eV) is at a lower energy than the substrate contact mode (2.17±0.02 eV), resulting in a redshift. Consequently the low energy mode is likely to increase with the increase in contact area, assuming homogeneous spherical NPs. The same trend is found in two isolated Au NPs for the 1%Au/TiO_2 sample (**Fig. S9**) that unexpectedly exhibit the same quantum yield as the 2% Au junction. Both Au NPs of 7.11 and 5.20 nm size display Δplasmon of (0.15 and 0.11) ±0.02 eV, which are (0.10 and 0.14) ±0.02 eV lower than the results for the 1%Au composite. This suggests that the Au NP -TiO_2 interface mode is of better quality in the 1%Au sample (of higher contact area) including a plasmon with a more pronounced oscillation. Such active surface plasmons can

enhance two possible mechanisms either the intensification of the electromagnetic field towards the interior of the SC or the hot electron injection from the Au NP structure (visible photon capacity) to the conduction band of TiO_2 (UV photon limited).[32,44,61]

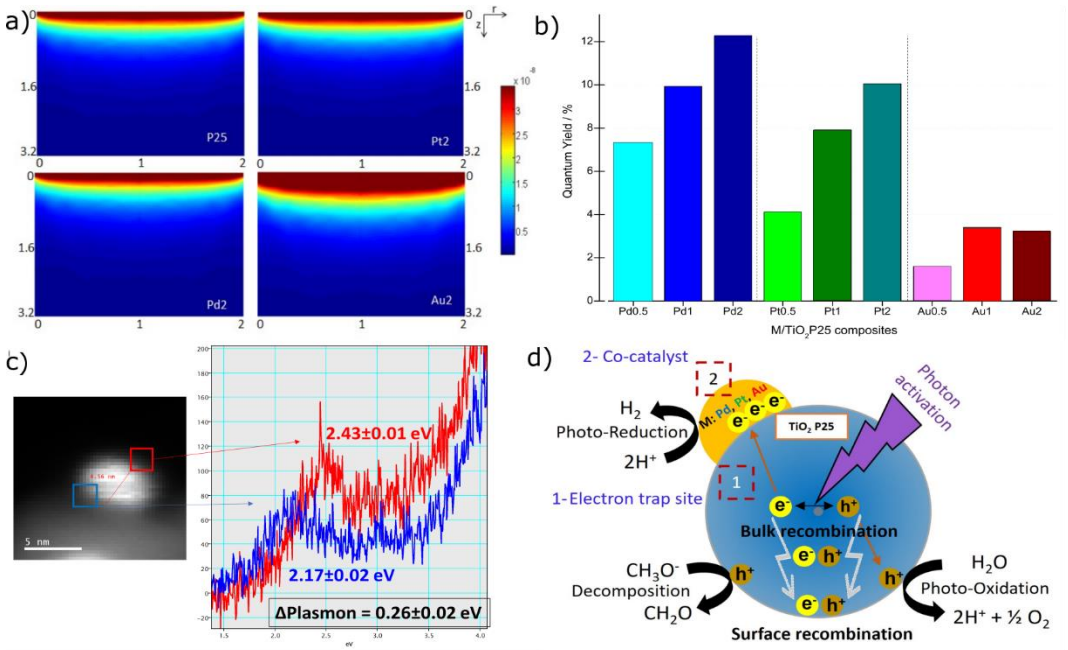

Figure 6. a) Local volumetric rate of photon absorption (Einstein cm^{-3} s^{-1}) of the catalytic suspension obtained for samples Pt2, Pd2 and Au2 and TiO_2 P25 reference. Local 2D photonic profile obtained for each r and z position **b)** Quantum yield results of all the composites **c)** EELS analysis on a 4,56 nm Au NP exhibiting its plasmon energy and modes on the 1%Au/TiO_2 junction **d)** Proposed mechanism for the M/TiO_2 junction including their charge electron-hole pathways and associated reactions

Figure 6d proposes an illustrative generalist mechanism of a punctual Schottky M/TiO_2 junction. The first step is the activation of the SC, after it is irradiated with a photon of equal or higher energy than its band gap, to form the exciton[10] (positive hole (h^+) in the valence band and an excited electron (e^-) in the conduction band, **equation 1**). Methanol is known to act as sacrificial agent or hole scavenger.[62,63] It oxidizes when subtracting the h^+ of the TiO_2 valence band resulting in a hydroxymethyl species and a proton (H^+)[64,65] (**equation 2**). There may also be another contribution of H^+ formation from the aqueous medium, driving the photo-oxidation of water in the presence of 2 h^+ given oxygen and H^+ (**equation 3**). Then the available H^+ in the presence of a single e^- from the TiO_2 CB drives the photo-reduction resulting in the desirable H_2 (**equation 4**).

$$TiO_2 + hv \rightarrow e_{CB}^- + h_{VB}^+ \text{ (exciton formation) (1)}$$
$$CH_3OH + h_{VB}^+ \rightarrow CH_2OH + H^+ \text{ (MeOH photo-oxidation) (2)}$$
$$H_2O + 2h_{VB}^+ \rightarrow \tfrac{1}{2}O_2 + 2H^+ \text{ (Water photo-oxidation) (3)}$$
$$e_{CB}^- + H^+ \rightarrow \tfrac{1}{2}H_2 \text{ (proton photo-reduction) (4)}$$

In summary, we develop a new compact reactor dedicated for HER under standard experimental conditions that has been commissioned by using Schottky (Pd, Pt, Au)/TiO_2 well-used materials in photocatalysis. H_2 photoproduction rates and quantum yields are almost one- and two-fold higher than literature average values, respectively, putting into evidence that the geometry and configuration setup brings the system one step closer to the ideal heat/mass/photonic profile, with low losses. The Schottky composites allow building novel structure-activity correlations. Insightful pieces of evidence are shown for the Au plasmon by coupling HRTEM, EELS, and UV-vis for the first time in literature, as the best of our knowledge. We stress two major conclusions: (A) the need for further development of compact and portable reactors to allow *in-situ* testing and coupling with key techniques such as TEM, XAS, XRD, among others and (B) the reporting of homogeneous criteria (IUPAC) for the accurate comparison of efficiencies across different studies and groups. We propose the use of this new photoreactor as a benchmark to foster further progress in process and chemical engineering, accelerate TRL, and as a strategy to overcome current limitations in scaling up photocatalysis.

Experimental section

1- Chemicals

AEROXIDE ® titanium dioxide P25 (TiO_2, 99%, Evonik Industries), Palladium (II) nitrate hydrate ($N_2O_6Pd*xH_2O$, ≥99,9%, Sigma Aldrich), Hexachloroplatinic acid hexahydrate ($H_2PtCl_6*6H_2O$, ≥37,5% Pt basis, Sigma Aldrich), Chloroauric acid trihydrate ($HAuCl_4*3H_2O$, ≥99,995% trace metal basis, Sigma Aldrich), sodium borohydride (≥98%, Sigma Aldrich), methanol (CH_3OH,

≥99.6%, Sigma Aldrich), ethanol (CH_3CH_2OH, ≥96%, Sigma Aldrich) were used without further purification.

2- Synthesis: noble metals anchoring onto TiO_2

(Pd, Pt, Au)/TiO_2 P25 samples were prepared by chemical reduction of the three different listed metal precursors.[66] TiO_2 P25, the support (350 mg) without further purification nor modification was dispersed in a methanol/ethanol mixture (91/9 v/v, 55 mL) with a bath sonicator (120W, 45 kHz) for 30 min, using 50% of the maximum sonication power. The calculated volume of a methanol/ethanol solution of the listed metal precursors solutions (1.5×10^{-2} mol L^{-1}) were added to achieve the chosen loadings, *i.e.,* 0.5, 1, and 2 wt.%. Sonication continues for 5 min, whereupon 5 mL of a fresh methanol/ethanol solution of $NaBH_4$ (10 mole fold higher than the initial precursor concentration) was added to guarantee full reduction of the cation metal.

3- Materials characterization

High-resolution transmission electron microscopy (HRTEM), TEM observations on individual deposited nanoparticles were performed on a JEOL1400 microscope operating at 80 kV. Samples were prepared according to a previously reported method.[67] Dilute aliquot of M/TiO_2 were prepared at 1 mg L^{-1} in ethanol. A drop of this mixture was deposited on a copper grid coated with carbon layer and dried at room temperature. The morphological parameters were measured over 200 individual particles using Fiji software.

Elemental analyses of the Schottky junctions were performed using ICP-AES. The limit of detection of the instrument was 0,1-0,2 mg L^{-1} for the chosen metals. Quantitative analysis of the noble metal component of the M/TiO_2 composites allowed the calculation of deposition yield

which are defined as the ratio between the actual deposited mass of the specific metal (deduced from ICP-AES analysis) and the mass of metal introduced during the deposition step (**Table S1**).

X-ray scattering (XRS) measurements were carried out on a Mo rotating anode generator (Rigaku Corp., Japan) equipped with a multilayer mirror (Osmic) delivering a monochromatic beam with incident wavelength $\lambda_{MoK\alpha}$ = 0.711 Å. Two-dimensional XRS patterns were collected on a MAR345 image plate detector (marXperts GmbH, Germany, pixel size = 150µm) placed at a distance of 150 mm from the samples. Powder samples were filled into borosilicate capillary tubes (WJM-Glas/Müller GmbH, DE) that were mounted on a goniometer head. Typical exposure time was 900s. Scattered intensity I as a function of the scattering vector modulus Q ($Q = 4\pi/\lambda \sin(\theta)$ where 2θ is the scattering angle) is obtained by angular integration over the 2D scattering patterns using homemade software. The Scherrer equation was used for the determination of the average crystallite size of the nanoparticles onto the support:

$$L = 0.9\lambda/\beta \cos\theta$$

with λ the incident wavelength and β the Full Width at Half the Maximum of the X-ray scattering peak (in radians) at a Bragg angle q.

Fourier-transform infrared spectroscopy. FTIR spectra were recorded on dry sample powders using a Nicolet iS50 (Thermo Scientific) spectrometer equipped with a KBr beam splitter and a DTGS/KBr detector. The transmission measurement in the range 4000−800 cm^{-1} was performed by averaging 200 scans at a resolution of 4 cm^{-1}. Transparent pressed pellets were prepared by mixing about 1.5 mg of dry powder sample with 150 mg of transparent KBr, to guarantee 1 wt. % of sample inside the final pellet.

UV-vis absorption spectra by Diffuse Reflectance Spectroscopy (DRS) were recorded on a Varian Cary 5E spectrophotometer from 300 to 650 nm. Diffuse reflectance spectra were converted into Kubelka-Munk units according to $F(R)= (1-R_d)^2/2R_d$, where $R_d= R_{sample}/R_{BaSO4}$, ($BaSO_4$ as the standard). For band gap calculation, Tauc plot was used and considering TiO_2 as indirect SC.

XPS analysis was performed using a Kratos Axis SUPRA XPS fitted with a monochromated Al kα X-ray source (1486.7 eV), a spherical sector analyzer and 3 multichannel resistive plate, 128 channel delay line detectors. All data was recorded at 150W and a spot size of 700 x 300 µm. Survey scans were recorded at a pass energy of 160 eV, and high-resolution scans recorded at a pass energy of 20 eV. Electronic charge neutralization was achieved using a magnetic immersion lens. Filament current = 0.27 A, charge balance = 3.3 V, filament bias = 3.8 V. All sample data was recorded at a pressure below 10-8 Torr and a room temperature of 294 K. Data was analyzed using CasaXPS (v2.3.19PR1.0). The energy shift due to electrostatic charging was subtracted using the carbon adventitious signal, *i.e.,* the C 1s peak located at 284.8 eV. Peaks were fit with a Shirley background prior to component analysis with the appropriate experimental sensitivity factors of the normalized photo ionization with modified Wagner factors.[68]

UPS analysis was performed using a Thermo NEXSA spectrometer fitted with a He (I) and He (II) lamp and dual neutralization flood gun. Such setup was equipped with a CLAM4 (MCD) hemispherical electron analyzer. Samples were drop cast from isopropanol onto copper foils prior to analysis. Spectra were recorded using a pass energy of 5 eV, a positive bias of 30V to avoid interference of the spectrometer threshold, a current of 50 mA and an energy step size of 0.1 eV.

Plasmon properties of Au NP@TiO_2 were studied by electron energy loss spectroscopy (EELS) in a modified NION monochromated Cs-corrected HERMES200 Scanning Transmission Electron

Microscope (STEM) fitted with a MerlinEM direct electron detector (Quantum DETECTORS). In this work, the experiments were performed at 60 kV, at a condenser convergent semi angle of 10 mrad with a typical EELS energy resolution (FWHM of ZLP) of 20 meV.

4- Photocatalytic tests

The photocatalytic activities of the (Pd, Pt, Au)/TiO_2 P25 Schottky junctions were evaluated against H_2 evolution reaction (HER) from methanolic aqueous solution (30% v/v) as sacrificial agent in a newly compact photoreactor setup (**Fig. 1**). H_2 production was performed in a compact stainless-steel photoreactor with 40 cm^3 and 65 cm^2 of volume and area, respectively using a quartz fused window (loss light intensity ≤5%) of 50x3 mm diameter and thickness containing 12 mL of methanol and 28 mL of Mili-Q deionized water. The 500 W Hg arc lamp from LOT Design (15,5 mW cm^{-2}, **Fig. S10**) was linked with a water filter circulating continuous tap water of 70 cm length allowing to pass 250-1000 nm to reduced unwanted heat increased and avoid thermal catalytic effect. The irradiance of such lamp was measured with a spectroradiometer (ILT950-UV-NIR, International Light Technologies). Prior to any experiment, residual oxygen was removed by nitrogen flushing. The photocatalytic tests were performed by suspending 40 mg of catalyst in 30% v/v of methanolic aqueous solution under continuous nitrogen flow at 60 mL min^{-1} and with mechanical stirring at 400 rpm. The reaction products were automated quantified online every 120 s by a μGC (990 model, Agilent) equipped with a thermal conductivity detector. The channel for H_2 quantification was using nitrogen as carrier gas flushing into a molecular sieve 5A SS (10m x 0,25mm x 30 μm). The injection system contained a pre-column and a backflush system for filtering undesirable humidity and separate more accurately the interest product while protecting the columns lifetime. A calibration curve was done using two Air liquide gas standards with 1 and 99,9% concentration of H_2.

5- Photonic profile description and quantum yield calculations

The photonic profile methodology is described in detail in the Support information (S1, **Fig. S1**). The quantum efficiency for all samples is obtained from the local volumetric rate of photon absorption calculated within the photonic model. The quantum yield is calculated as following:

$$\eta_q(\%) = 100 \times \frac{2 \times r\ (\text{mol m}^{-3}\text{s}^{-1})}{< e^{a,v} >\ (\text{Einstein m}^{-3}\text{s}^{-1})}$$

This equation considers two electrons transfer to reduce two protons into one H_2 molecule.

Acknowledgements

EP and PJC acknowledge the financial support of the French ANR agency (ANR) under grant agreement ANR-18-CE09-0001 (C3PO) and the CNRS through the International Emerging Actions program (no. 08216). The results used the Imagerie-Gif core facility supported by l'Agence Nationale de la Recherche (ANR-11-EQPX-0029/Morphoscope, ANR-10-INBS-04/FranceBioImaging; ANR-11-IDEX-0003-02/ Saclay Plant Sciences). The X-ray photoelectron (XPS) data collection was performed at the EPSRC National Facility for XPS ("HarwellXPS"), operated by Cardiff University and UCL, under Contract No. PR16195. The authors acknowledge financial support from the CNRS-CEA "METSA" French network (FR CNRS 3507) on the platform STEM-LPS. This work has received support from the French State through the National Agency for Research under the program of future investment EQUIPEX TEMPOS-CHROMATEM with the reference ANR-10-EQPX-50. The authors thank Stéphane Cabaret (LPS/CNRS, Orsay) for the design and realization of the photoreactor, Anne Boos (IPHC/ECPM, Strasbourg) for the ICP-AES analyses and Fabrice Gros (CNRS/U. Clermont Ferrand) for fruitful reactor details discussions.

References

(1) (IEA), I. E. A. Key World Energy Statistics 2016 https://www.iea.org/publications/freepublications/publication/key-world-energy-statistics.html (accessed Dec 28, 2016).

(2) Perez, R.; Perez, M. A Fundamental Look at Supply Side Energy Reserves for the Planet. *Int. Energy Agency Sol. Heat. Cool. Program. Sol. Updat.* **2009**, *50*, 4–5.

(3) Kruger, P. Electric Power Required in the World by 2050 with Hydrogen Fuel Production—Revised. *Int. J. Hydrogen Energy* **2005**, *30* (15), 1515–1522. https://doi.org/10.1016/J.IJHYDENE.2005.04.003.

(4) The Future of Solar Energy | MIT Energy Initiative http://energy.mit.edu/publication/future-solar-energy/ (accessed May 10, 2018).

(5) Lewis, N. S.; Crabtree, G.; Nozik, A. J.; Wasielewski, M. R.; Alivisatos, P.; Kung, H.; Tsao, J.; Chandler, E.; Walukiewicz, W.; Spitler, M.; Ellingson, R.; Overend, R.; Mazer, J.; Gress, M.; Horwitz, J.; Ashton, C.; Herndon, B.; Shapard, L.; Nault, R. M. *Basic Research Needs for Solar Energy Utilization. Report of the Basic Energy Sciences Workshop on Solar Energy Utilization, April 18-21, 2005*; 2005. https://doi.org/10.2172/899136.

(6) Novel Hydrogen Carriers | Department of Energy https://www.energy.gov/eere/fuelcells/novel-hydrogen-carriers (accessed Jan 23, 2022).

(7) Melchionna, M.; Fornasiero, P. Updates on the Roadmap for Photocatalysis. *ACS Catal.* **2020**, *10* (10), 5493–5501. https://doi.org/10.1021/acscatal.0c01204.

(8) (IEA), I. E. A. *Technology Roadmap Hydrogen and Fuel Cells*; 2015.

(9) Fujishima, A.; Honda, K. Electrochemical Photolysis of Water at a Semiconductor Electrode. *Nature* **1972**, *238* (5358), 37–38. https://doi.org/10.1038/238037a0.

(10) Takanabe, K. Photocatalytic Water Splitting: Quantitative Approaches toward Photocatalyst by Design. *ACS Catal.* **2017**, *7* (11), 8006–8022. https://doi.org/10.1021/acscatal.7b02662.

(11) Li, J.; Jiménez-Calvo, P.; Paineau, E.; Ghazzal, M. N. Metal Chalcogenides Based Heterojunctions and Novel Nanostructures for Photocatalytic Hydrogen Evolution. *Catalysts*. MDPI AG January 1, 2020, p 89. https://doi.org/10.3390/catal10010089.

(12) Wang, Y.; Vogel, A.; Sachs, M.; Sebastian Sprick, R.; Wilbraham, L.; A Moniz, S. J.; Godin, R.; Zwijnenburg, M. A.; Durrant, J. R.; Cooper, A. I.; Tang, J. Current Understanding and Challenges of Solar-Driven Hydrogen Generation Using Polymeric Photocatalysts. https://doi.org/10.1038/s41560-019-0456-5.

(13) Sundar, K. P.; Kanmani, S. Progression of Photocatalytic Reactors and It's Comparison: A Review. *Chemical Engineering Research and Design*. Institution of Chemical Engineers February 1, 2020, pp 135–150. https://doi.org/10.1016/j.cherd.2019.11.035.

(14) Muñoz-Batista, M. J.; Ballari, M. M.; Kubacka, A.; Alfano, O. M.; Fernández-García, M. Braiding Kinetics and Spectroscopy in Photo-Catalysis: The Spectro-Kinetic Approach. *Chem. Soc. Rev.* **2019**, *48* (2), 637–682. https://doi.org/10.1039/C8CS00108A.

(15) Muñoz-Batista, M. J.; Rodríguez-Padrón, D.; Puente-Santiago, A. R.; Kubacka, A.; Luque, R.; Fernández-García, M. Sunlight-Driven Hydrogen Production Using an Annular Flow Photoreactor and g-C3N4-Based Catalysts. *ChemPhotoChem* **2018**, *2* (10), 870–877.

https://doi.org/10.1002/CPTC.201800064.

(16) Khan, A. A.; Tahir, M. Recent Advancements in Engineering Approach towards Design of Photo-Reactors for Selective Photocatalytic CO2 Reduction to Renewable Fuels. *Journal of CO2 Utilization*. Elsevier Ltd January 1, 2019, pp 205–239. https://doi.org/10.1016/j.jcou.2018.12.008.

(17) Low, J.; Yu, J.; Jaroniec, M.; Wageh, S.; Al-Ghamdi, A. A. Heterojunction Photocatalysts. *Advanced Materials*. Wiley-VCH Verlag May 24, 2017. https://doi.org/10.1002/adma.201601694.

(18) Marschall, R. Semiconductor Composites: Strategies for Enhancing Charge Carrier Separation to Improve Photocatalytic Activity. *Adv. Funct. Mater.* **2014**, *24* (17), 2421–2440. https://doi.org/10.1002/adfm.201303214.

(19) Jiménez-Calvo, P.; Caps, V.; Keller, V. Plasmonic Au-Based Junctions onto TiO2, GC3N4, and TiO2-GC3N4 Systems for Photocatalytic Hydrogen Production: Fundamentals and Challenges. *Renew. Sustain. Energy Rev.* **2021**, *149*, 111095. https://doi.org/10.1016/J.RSER.2021.111095.

(20) Nakata, K.; Fujishima, A. TiO_2 Photocatalysis: Design and Applications. *J. Photochem. Photobiol. C Photochem. Rev.* **2012**, *13* (3), 169–189. https://doi.org/10.1016/J.JPHOTOCHEMREV.2012.06.001.

(21) O'Regan, B.; Grätzel, M. A Low-Cost, High-Efficiency Solar Cell Based on Dye-Sensitized Colloidal TiO_2 Films. *Nature* **1991**, *353* (6346), 737–740. https://doi.org/10.1038/353737a0.

(22) Schottky, W. Halbleitertheorie Der Sperrschicht. *Naturwissenschaften 1938 2652* **1938**, *26* (52), 843–843. https://doi.org/10.1007/BF01774216.

(23) Ingram, D. B.; Linic, S. Water Splitting on Composite Plasmonic-Metal/Semiconductor Photoelectrodes: Evidence for Selective Plasmon-Induced Formation of Charge Carriers near the Semiconductor Surface. *J. Am. Chem. Soc.* **2011**, *133* (14), 5202–5205. https://doi.org/10.1021/ja200086g.

(24) Wang, M.; Ye, M.; Iocozzia, J.; Lin, C.; Lin, Z.; Wang, M.; Iocozzia, J.; Lin, Z.; Lin, C.; Ye, M. Plasmon-Mediated Solar Energy Conversion via Photocatalysis in Noble Metal/Semiconductor Composites. *Adv. Sci.* **2016**, *3* (6), 1600024. https://doi.org/10.1002/ADVS.201600024.

(25) Brancho, J. J.; Bartlett, B. M. Challenges in Co-Alloyed Titanium Oxynitrides, a Promising Class of Photochemically Active Materials. *Chem. Mater.* **2015**, *27* (21), 7207–7217. https://doi.org/10.1021/acs.chemmater.5b02357.

(26) Kubacka, A.; Fernández-García, M.; Colón, G. Advanced Nanoarchitectures for Solar Photocatalytic Applications. *Chem. Rev.* **2011**, *112* (3), 1555–1614. https://doi.org/10.1021/CR100454N.

(27) Chen, X.; Li, C.; Grätzel, M.; Kostecki, R.; Mao, S. S. Nanomaterials for Renewable Energy Production and Storage. *Chem. Soc. Rev.* **2012**, *41* (23), 7909. https://doi.org/10.1039/c2cs35230c.

(28) Nazeeruddin, M. K.; Baranoff, E.; Grätzel, M. Dye-Sensitized Solar Cells: A Brief Overview. *Sol. Energy* **2011**, *85* (6), 1172–1178.

https://doi.org/10.1016/j.solener.2011.01.018.

(29) Bai, S.; Zhang, N.; Gao, C.; Xiong, Y. Defect Engineering in Photocatalytic Materials. *Nano Energy*. https://doi.org/S2211285518306207.

(30) Ola, O.; Maroto-Valer, M. M. Review of Material Design and Reactor Engineering on TiO2 Photocatalysis for CO2 Reduction. *J. Photochem. Photobiol. C Photochem. Rev.* **2015**, *24*, 16–42. https://doi.org/10.1016/J.JPHOTOCHEMREV.2015.06.001.

(31) Rycenga, M.; Cobley, C. M.; Zeng, J.; Li, W.; Moran, C. H.; Zhang, Q.; Qin, D.; Xia, Y. Controlling the Synthesis and Assembly of Silver Nanostructures for Plasmonic Applications. *Chem. Rev.* **2011**, *111* (6), 3669–3712. https://doi.org/10.1021/cr100275d.

(32) Dubi, Y.; Sivan, Y. "Hot" Electrons in Metallic Nanostructures—Non-Thermal Carriers or Heating? *Light Sci. Appl.* **2019**, *8* (1), 2047–7538. https://doi.org/10.1038/s41377-019-0199-x.

(33) Trasatti, S. Work Function, Electronegativity, and Electrochemical Behaviour of Metals: III. Electrolytic Hydrogen Evolution in Acid Solutions. *J. Electroanal. Chem. Interfacial Electrochem.* **1972**, *39* (1), 163–184. https://doi.org/10.1016/S0022-0728(72)80485-6.

(34) Parsons, R. The Rate of Electrolytic Hydrogen Evolution and the Heat of Adsorption of Hydrogen. *Trans. Faraday Soc.* **1958**, *54* (0), 1053–1063. https://doi.org/10.1039/TF9585401053.

(35) Dahi, G.; Eskandari, A.; Dauchet, J.; Gros, F.; Roudet, M.; Cornet, J.-F. A Novel Experimental Bench Dedicated to the Accurate Radiative Analysis of Photoreactors: The

Case Study of CdS Catalyzed Hydrogen Production from Sacrificial Donors. *Chem. Eng. Process. Process Intensif.* **2015**, *98*, 174–186. https://doi.org/10.1016/j.cep.2015.09.015.

(36) Schwarze, M.; Stellmach, D.; Schröder, M.; Kailasam, K.; Reske, R.; Thomas, A.; Schomäcker, R. Quantification of Photocatalytic Hydrogen Evolution. *Phys. Chem. Chem. Phys.* **2013**, *15* (10), 3466–3472. https://doi.org/10.1039/C3CP50168J.

(37) Romero, R. L.; Alfano, O. M.; Cassano, A. E. Cylindrical Photocatalytic Reactors. Radiation Absorption and Scattering Effects Produced by Suspended Fine Particles in an Annular Space. *Ind. Eng. Chem. Res.* **1997**, *36* (8), 3094–3109. https://doi.org/10.1021/IE960664A.

(38) Duderstadt, J. J.; Martin, W. R. *Transport Theory*; John Wiley & Sons: New York, 1979.

(39) Hosseinpour, S.; Tang, F.; Wang, F.; Livingstone, R. A.; Schlegel, S. J.; Ohto, T.; Bonn, M.; Nagata, Y.; Backus, E. H. G. Chemisorbed and Physisorbed Water at the TiO2/Water Interface. *J. Phys. Chem. Lett.* **2017**, *8* (10), 2195–2199. https://doi.org/10.1021/ACS.JPCLETT.7B00564/SUPPL_FILE/JZ7B00564_SI_001.PDF.

(40) Of, J.; Фізики, N.-A. E. P. Ж. H.-T. E. A Simple Approach on Synthesis of TiO2 Nanoparticles and Its Application in Dye Sensitized Solar Cells. *Том* **2017**, *9* (6pp), 4005. https://doi.org/10.21272/jnep.9(4).04005.

(41) Praveen, P.; Viruthagiri, G.; Mugundan, S.; Shanmugam, N. Structural, Optical and Morphological Analyses of Pristine Titanium Di-Oxide Nanoparticles – Synthesized via Sol–Gel Route. *Spectrochim. Acta Part A Mol. Biomol. Spectrosc.* **2014**, *117*, 622–629. https://doi.org/10.1016/J.SAA.2013.09.037.

(42) Ohtani, B.; Prieto-Mahaney, O. O.; Li, D.; Abe, R. What Is Degussa (Evonik) P25? Crystalline Composition Analysis, Reconstruction from Isolated Pure Particles and Photocatalytic Activity Test. *J. Photochem. Photobiol. A Chem.* **2010**, *216* (2–3), 179–182. https://doi.org/10.1016/j.jphotochem.2010.07.024.

(43) Masao, K.; Okura, I. *Photocatalysis: Science and Technology*, I.; Springer: Berlin, Heidelberg, 2002. https://doi.org/10.1016/S1010-6030(03)00234-X.

(44) Jiménez-Calvo, P. I. Synthesis, Characterization, and Performance of g-C3N4 Based Materials Decorated with Au Nanoparticles for (Photo) Catalytic Applications, Université de Strasbourg, 2019.

(45) Li, N.; Zhao, P.; Astruc, D. Anisotropic Gold Nanoparticles: Synthesis, Properties, Applications, and Toxicity. *Angewandte Chemie - International Edition*. John Wiley & Sons, Ltd February 10, 2014, pp 1756–1789. https://doi.org/10.1002/anie.201300441.

(46) Pourbaix, M. *Atlas of Electrochemical Equilibria in Aqueous Solutions,* [1st English ed.].; Pergamon Press: Oxford ;New York, 1966.

(47) Kelly, K. L.; Coronado, E.; Zhao, L. L.; Schatz, G. C. The Optical Properties of Metal Nanoparticles: The Influence of Size, Shape, and Dielectric Environment. **2003**. https://doi.org/10.1021/jp026731y.

(48) Shiraishi, Y.; Yasumoto, N.; Imai, J.; Sakamoto, H.; Tanaka, S.; Ichikawa, S.; Ohtani, B.; Hirai, T. Quantum Tunneling Injection of Hot Electrons in Au/TiO_2 Plasmonic Photocatalysts. *Nanoscale* **2017**, *9* (24), 8349–8361. https://doi.org/10.1039/C7NR02310C.

(49) Linic, S.; Christopher, P.; Ingram, D. B. Plasmonic-Metal Nanostructures for Efficient Conversion of Solar to Chemical Energy. *Nat. Mater.* **2011**, *10* (12), 911–921. https://doi.org/10.1038/nmat3151.

(50) Bingham, M.; Mills, A. Photonic Efficiency and Selectivity Study of M (M=Pt, Pd, Au and Ag)/TiO2 Photocatalysts for Methanol Reforming in the Gas Phase. *J. Photochem. Photobiol. A Chem.* **2020**, *389*, 112257. https://doi.org/10.1016/J.JPHOTOCHEM.2019.112257.

(51) Michaelson, H. B. Work Functions of the Elements. *J. Appl. Phys.* **1950**, *21* (6), 536–540. https://doi.org/10.1063/1.1699702.

(52) Sanchez, M. G.; Gazquez, J. L. Oxygen Vacancy Model in Strong Metal-Support Interaction. *J. Catal.* **1987**, *104* (1), 120–135. https://doi.org/10.1016/0021-9517(87)90342-3.

(53) Cha, G.; Hwang, I.; Hejazi, S.; Dobrota, A. S.; Pašti, I. A.; Osuagwu, B.; Kim, H.; Will, J.; Yokosawa, T.; Badura, Z.; Kment, Š.; Mohajernia, S.; Mazare, A.; Skorodumova, N. V.; Spiecker, E.; Schmuki, P. As a Single Atom Pd Outperforms Pt as the Most Active Co-Catalyst for Photocatalytic H2 Evolution. *iScience* **2021**, *24* (8), 102938. https://doi.org/10.1016/J.ISCI.2021.102938.

(54) Jiménez-Calvo, P.; Caps, V.; Ghazzal, M. N.; Colbeau-Justin, C.; Keller, V. Au/TiO_2(P25)-GC_3N_4 Composites with Low GC_3N_4 Content Enhance TiO_2 Sensitization for Remarkable H_2 Production from Water under Visible-Light Irradiation. *Nano Energy* **2020**, *75*, 104888. https://doi.org/10.1016/j.nanoen.2020.104888.

(55) Muñoz-Batista, M. J.; Motta Meira, D.; Colón, G.; Kubacka, A.; Fernández-García, M. Phase-Contact Engineering in Mono- and Bimetallic Cu-Ni Co-Catalysts for Hydrogen Photocatalytic Materials. *Angew. Chemie Int. Ed.* **2018**, *57* (5), 1199–1203. https://doi.org/10.1002/ANIE.201709552.

(56) Caudillo-Flores, U.; Muñoz-Batista, M. J.; Fernández-García, M.; Kubacka, A. Bimetallic Pt-Pd Co-Catalyst Nb-Doped TiO2 Materials for H2 Photo-Production under UV and Visible Light Illumination. *Appl. Catal. B Environ.* **2018**, *238*, 533–545. https://doi.org/10.1016/J.APCATB.2018.07.047.

(57) Priebe, J. B.; Radnik, J.; Lennox, A. J. J.; Pohl, M.-M.; Karnahl, M.; Hollmann, D.; Grabow, K.; Bentrup, U.; Junge, H.; Beller, M.; Brückner, A. Solar Hydrogen Production by Plasmonic Au–TiO2 Catalysts: Impact of Synthesis Protocol and TiO2 Phase on Charge Transfer Efficiency and H2 Evolution Rates. *ACS Catal.* **2015**, *5* (4), 2137–2148. https://doi.org/10.1021/CS5018375.

(58) Fontelles-Carceller, O.; Muñoz-Batista, M. J.; Conesa, J. C.; Fernández-García, M.; Kubacka, A. UV and Visible Hydrogen Photo-Production Using Pt Promoted Nb-Doped TiO2 Photo-Catalysts: Interpreting Quantum Efficiency. *Appl. Catal. B Environ.* **2017**. https://doi.org/10.1016/j.apcatb.2017.05.022.

(59) Nie, J.; Schneider, J.; Sieland, F.; Zhou, L.; Xia, S.; Bahnemann, D. W. New Insights into the Surface Plasmon Resonance (SPR) Driven Photocatalytic H2 Production of Au–TiO2. *RSC Adv.* **2018**, *8* (46), 25881–25887. https://doi.org/10.1039/C8RA05450A.

(60) Kociak, M.; Stéphan, O. Mapping Plasmons at the Nanometer Scale in an Electron

Microscope. *Chemical Society Reviews*. Royal Society of Chemistry June 7, 2014, pp 3865–3883. https://doi.org/10.1039/c3cs60478k.

(61) Ratchford, D. C. Plasmon-Induced Charge Transfer: Challenges and Outlook. *ACS Nano* **2019**, *13* (12), 13610–13614. https://doi.org/10.1021/acsnano.9b08829.

(62) Connelly, K.; Wahab, A. K.; Idriss, H. Photoreaction of Au/TiO_2 for Hydrogen Production from Renewables: A Review on the Synergistic Effect between Anatase and Rutile Phases of TiO2. *Mater. Renew. Sustain. Energy* **2012**, *1* (1), 1–12. https://doi.org/10.1007/s40243-012-0003-9.

(63) Pellegrin, Y.; Odobel, F. Sacrificial Electron Donor Reagents for Solar Fuel Production. *Comptes Rendus Chim.* **2017**, *20* (3), 283–295. https://doi.org/10.1016/j.crci.2015.11.026.

(64) Schneider, J. T.; Firak, D. S.; Ribeiro, R. R.; Peralta-Zamora, P. Use of Scavenger Agents in Heterogeneous Photocatalysis: Truths, Half-Truths, and Misinterpretations. *Phys. Chem. Chem. Phys.* **2020**, *22* (27), 15723–15733. https://doi.org/10.1039/D0CP02411B.

(65) Marouazi, H. El; Jiménez-Calvo, P.; Breniaux, E.; Colbeau-Justin, C.; Janowska, I.; Keller, V. Few Layer Graphene/TiO2 Composites for Enhanced Solar-Driven H2 Production from Methanol. *ACS Sustain. Chem. Eng.* **2021**, *9* (10), 3633–3646. https://doi.org/10.1021/ACSSUSCHEMENG.0C06808.

(66) Jiménez-Calvo, P.; Marchal, C.; Cottineau, T.; Caps, V.; Keller, V. Influence of the Gas Atmosphere during the Synthesis of G-C<inf>3</Inf>N<inf>4</Inf> for Enhanced Photocatalytic H<inf>2</Inf> Production from Water on Au/g-C<inf>3</Inf>N<inf>4</Inf> Composites. *J. Mater. Chem. A* **2019**, *7* (24).

https://doi.org/10.1039/c9ta01734h.

(67) Paineau, E.; Monet, G.; Peyre, V.; Goldmann, C.; Rouzière, S.; Launois, P. [ASAP] Colloidal Stability of Imogolite Nanotube Dispersions: A Phase Diagram Study. *Langmuir*. https://doi.org/10.1021/acs.langmuir.9b01922.

(68) Wagner, C. D.; Davis, L. E.; Zeller, M. V.; Taylor, J. A.; Raymond, R. H.; Gale, L. H. Empirical Atomic Sensitivity Factors for Quantitative Analysis by Electron Spectroscopy for Chemical Analysis. *Surf. Interface Anal.* **1981**, *3* (5), 211–225. https://doi.org/10.1002/SIA.740030506.